Nanotechnology

PAPER • OPEN ACCESS

Structural, optical, and mechanical properties of TiO_2 nanolaminates

To cite this article: Lilit Ghazaryan *et al* 2021 *Nanotechnology* **32** 095709

View the article online for updates and enhancements.

IOP ebooks™

Bringing together innovative digital publishing with leading authors from the global scientific community.

Start exploring the collection–download the first chapter of every title for free.

This content was downloaded from IP address 139.17.31.57 on 03/02/2021 at 07:16

OPEN ACCESS
IOP Publishing

Nanotechnology

Nanotechnology **32** (2021) 095709 (14pp)

https://doi.org/10.1088/1361-6528/abcbc1

Structural, optical, and mechanical properties of TiO_2 nanolaminates

Lilit Ghazaryan[1,4], Shiti Handa[1,4], Paul Schmitt[1,2], Vivek Beladiya[1], Vladimir Roddatis[3,5], Andreas Tünnermann[1,2] and Adriana Szeghalmi[1,2]

[1] Institute of Applied Physics, Abbe Center of Photonics, Friedrich Schiller University Jena, Germany
[2] Fraunhofer Institute for Applied Optics and Precision Engineering IOF, Jena, Germany
[3] Institute of Materials Physics, University of Göttingen, Germany

E-mail: adriana.szeghalmi@iof.fraunhofer.de

Received 29 July 2020, revised 5 October 2020
Accepted for publication 18 November 2020
Published 10 December 2020

Abstract

The structural, optical, and mechanical properties of TiO_2 nanolaminate films grown by plasma-enhanced atomic layer deposition are discussed. Several TiO_2/Al_2O_3 and TiO_2/SiO_2 compositions have been investigated to study the effect of the relative number of ALD oxide cycles on the film properties to obtain a high refractive index coating with low optical losses, low roughness, and low mechanical stress. The formation of crystalline TiO_2 observed at high deposition temperature, or film thickness was inhibited by periodically introducing ultra-thin amorphous layers into the film. Only 4 ALD cycles of Al_2O_3 (corresponding to ca. 0.5 nm) between 335 ALD cycles of TiO_2 (ca. 11 nm) form a closed, distinct layer suppressing the crystallization in TiO_2 film. Consequently, the roughness of the pure TiO_2 film is reduced from ca. 20 nm rms to 1 nm rms in the 335/4 nanolaminate, with only a slight decrease of the refractive index from 2.46 to 2.44 in 100 nm pure TiO_2 and the nanolaminate, respectively. The refractive indices of the nanolaminates in various compositions vary between 2.38 and 2.50 at 632 nm, and the corresponding optical losses from the films are low. The mechanical stress was reduced to about 140 MPa in several TiO_2/Al_2O_3 nanolaminates; however, lower mechanical stress has not been obtained with the studied compositions. The nanolaminate structure is preserved up to 600 °C annealing temperature. After annealing at 800 °C, the individual layers interdiffuse into each other so that no distinct nanolaminate structure is detected. By using TiO_2/Al_2O_3 nanolaminates with reduced mechanical stress, a narrow bandpass filter was realized on various substrates, including half-ball and aspherical lenses.

Supplementary material for this article is available online

Keywords: titania (TiO_2), nanolaminates, plasma enhanced atomic layer deposition (PEALD), mechanical stress, optical coatings, narrow bandpass filter (NBF), interference coatings

(Some figures may appear in colour only in the online journal)

[4] These authors contributed equally to the work.
[5] Current address: German Research Centre for Geosciences GFZ, Helmholtz Centre Potsdam, Germany.

Original content from this work may be used under the terms of the Creative Commons Attribution 4.0 licence. Any further distribution of this work must maintain attribution to the author(s) and the title of the work, journal citation and DOI.

1. Introduction

Titanium dioxide (TiO_2) thin films have extensively been investigated as non-toxic, chemically stable, low-cost semi-conducting coatings in a wide area of applications such as solar cells [1], photocatalysis [2], batteries [3], wire grid polarizers [4], sensors [5], etc. TiO_2 is considered to be a promising candidate among dielectrics as high refractive index optical coating in multilayer optical systems [6, 7].

However, the use of TiO_2 for optical coatings is challenging due to the formation of polycrystalline thin films during the deposition processes [8].

The important material properties of the coatings are, among others, the density, the refractive index, the surface roughness, and the mechanical stress. The mechanical stress of thin coatings is essential for numerous applications, such as in microelectromechanical systems (MEMS), semi-conductors, or optical devices [9]. Especially for the applications where thick, multilayer stacks with an overall thickness above 1 μm are required, the residual mechanical stress in the films plays a crucial role. High and low refractive index multilayer stacks, e.g. broadband antireflection coatings, dichroic mirrors, and narrow bandpass filters (NBF) are examples of such coatings in optics. High residual stress in single layers leads to severe cracking of the films in the optical element [10]. Hence, further improvement of the mechanical properties of single layers is essential for such optical coatings.

Among other deposition techniques, atomic layer deposition (ALD) is considered to be the method of choice for conformal coatings on highly curved, porous, micro- or nanostructured substrates with precise thickness control [11–17]. The surface-limiting nature of the chemical reactions during the ALD process allows the deposition of not only pure materials but also composites and nanolaminates with precisely controlled thickness and composition [18, 19]. The low deposition rate of the ALD, which has been considered as the main drawback of this technology, is nowadays successfully overcome by using high-speed spatial ALD reactors. Such industrial ALD tools allow the combination of ALD features with high throughput [20–23].

The deposition of high quality, smooth, and mechanically stress-free thin films by ALD is necessary for applications in optics, MEMS, barrier and protective coatings, etc [24–26]. For optical applications, the growth of an amorphous film is necessary to avoid optical losses due to scattering or stray light. Depending on the film thickness and deposition temperature, TiO_2 exhibits crystalline phases during the ALD growth [27, 28]. The crystallization of TiO_2 films can be controlled by reducing the deposition temperature and the power of the plasma during the plasma-enhanced ALD (PEALD) process [8, 29, 30]. However, reducing the deposition temperature or the plasma power typically leads to a decreased film density and, consequently, lower refractive index.

Another approach of inhibiting the crystal growth in the TiO_2 films is the periodic introduction of thin amorphous layers such as Al_2O_3 or SiO_2 into TiO_2 films [31–33]. With this approach, the crystallinity of TiO_2 coatings can be suppressed, whereas the quality of the film is maintained. These interlayers also reduce surface roughness by suppressing the development of gross facets, thereby interrupting the crystalline growth repeatedly. Several studies about ALD TiO_2/Al_2O_3 nanolaminates have been carried out by tailoring and adjusting the film properties for various applications, such as in capacitors [34], for encapsulation of organic diodes [35, 36], in solar cells [37], as gate dielectrics [38, 39], etc [40]. However, only a few studied TiO_2/Al_2O_3 nanolaminate properties with respect to their optical applications in multilayer stacks [31, 41, 42]. These studies investigated thermally deposited nanolaminates, and only a few investigated in detail the optical and mechanical properties of these films.

This article reports on the structural, mechanical, and optical properties of TiO_2 nanolaminates with Al_2O_3 and SiO_2 deposited by PEALD. Amorphous SiO_2 has been applied besides Al_2O_3 for a better understanding of how amorphous oxides influence the structural, mechanical, and optical properties of nanolaminates (i) using PEALD, (ii) depending on the mechanical stress of individual layers, and (iii) depending on the degree of intermixing of the components. This work aims to present a detailed quantitative analysis of TiO_2 nanolaminates to achieve thin film coatings with essential properties for optical applications: high refractive index, low residual stress, low optical losses, and low surface roughness. Additionally, extensive studies on the thermal stability of the nanolaminates have been carried out based on x-ray diffraction (XRD), x-ray reflectivity (XRR), spectroscopic ellipsometry (SE), and mechanical stress measurements of annealed thin films. While our focus is on developing composites with enhanced properties for optical coatings, the findings presented here can be transferred towards other applications.

Furthermore, taking advantage of the superior optical and mechanical properties of nanolaminates, we demonstrate a NBF of an interference multilayer with Al_2O_3/TiO_2 nanolaminates as high (H) and SiO_2 as low (L) refractive index materials, respectively. The NBF has been realized on various substrates, including ball, half-ball and aspherical lenses.

2. Methods

2.1. Atomic layer deposition (ALD)

Single and nanolaminate films were deposited using the Oxford Instruments Plasma Technology (Bristol, UK) OpAL ALD open-load system. Titanium isopropoxide, TTIP (CAS No. 546-68-9, 98%, Strem Chemicals, Strasbourg, France), trimethyl-aluminum, TMA (CAS No. 75-24-1, 98%, Strem Chemicals, Strasbourg, France), and tris(dimethyl-amino) silane, TDMAS (CAS No. 15112-89-7, 99%, SAFC, Wirral, UK) served as metalorganic precursors for TiO_2, Al_2O_3, and SiO_2, respectively. Oxygen (99.99%) plasma was used as an oxidizing agent. The plasma power was 300 W with an oxygen flow rate of 50 standard cubic centimeters (sccm), resulting in a pressure of approximately 0.5 mbar in the ALD chamber during the process. The process parameters and the growth rates per cycle (GPC) of these films are summarized in table 1. Double side polished 75 mm diameter Si-wafers, fused silica (FS), BK7, and polycarbonate (PC) served as substrates for various characterization methods.

The PEALD nanolaminates have been deposited with various compositions by alternating the ALD cycles of the materials. The nanolaminates are named as the ratio of the number of ALD cycles of materials. The first number denotes the number of TiO_2 cycles, and the second is the number of Al_2O_3 or SiO_2 cycles. These bilayers were repeated as

Table 1. PEALD process parameters and GPC at 100 °C.

Oxide	Precursor pulse (s)	Purge (s)	Plasma pulse (s)	Plasma purge (s)	GPC (Å/cycle) ±0.05
TiO_2	1.5	7	6	4	0.30
Al_2O_3	0.03	5	5	2.5	1.20
SiO_2	0.4[a]	5	5	5	1.20

[a] 4 s of hold step of the precursor is additionally required after precursor pulse.

necessary. The nanolaminates were capped with TiO_2 cycles to reach a film thickness of approximately 200 nm.

The NBF comprises 23 alternating layers of TiO_2/Al_2O_3 nanolaminate and SiO_2, including a SiO_2 spacer layer in the middle. The overall physical thickness is approximately 1.8 μm. To perceive the difference in the mechanical performance of such a complex coating depending on the substrate, the NBF has been realized on various substrates including ball and half-ball lenses (diameters of 10 and 4 mm, respectively), a large asphere (50 mm diameter and 25 mm height), plane FS and BK7 glasses and Si substrates.

2.2. Characterization methods

The refractive indices and thicknesses of the films grown on Si wafer were determined on p-type (100) Si substrates using SE measurements (M2000 ellipsometer, J A Woollam Inc, Bristol, UK) in the spectral range from 400 to 1700 nm. The optical constants of the films were calculated by fitting the ellipsometry measured data of Ψ and Δ with the Cauchy model in the spectral range of 400–1000 nm, using CompleteEASE software. The thickness non-uniformity of the deposition was determined as $(d_{\max} - d_{\min}/2d_{\text{average}})$ * 100% on five Si substrates placed one in the middle and four on the diameter of a six-inch circle.

Refractive indices, optical losses, and homogeneity of films grown on borosilicate BK7 glass, fused silica, and polycarbonate (PC) substrates were analyzed using the dual-beam ratio recording spectrophotometer Lambda 900 from Perkin Elmer™. The reflectance and transmittance spectra additionally allowed the determination of the film thickness and optical constants from analysis using the Film Wizard software (Scientific Computing International, SCI) based on a Cauchy model. Since the thickness of the Al_2O_3 or SiO_2 interlayers is much smaller than the wavelength of the light, nanolaminates have been treated as effective media for the analysis. The refractive index is being reported at 632.8 nm wavelength throughout the article.

The mechanical stress values of the ALD films were measured using the wafer curvature method with a FLX 2320 equipment (KLA-Tencor GmbH, San Jose, USA). The instrument measures the curvature of the pre and post deposited wafer, yielding the stress. The stress value is calculated by using Stoney's equation [43] (see equation (1)), where E_s is the Young's modulus, ϑ_s is Poisson's ratio of the substrate, R_s and R_f are the radii of curvature of the substrate before and after coating, and t_s and t_f are the thicknesses of the substrate and the film, respectively. All measurements were performed at least 3 times and the changes in stress were monitored for a period of several weeks. Experimental error is attributed to the uncertainty of substrate and film thicknesses in addition to instrumental error from the wafer curvature. Positive mechanical stress values in this article correspond to tensile stress, whereas negative values to compressive.

$$\sigma = \frac{1}{6}\frac{E_s}{(1-\vartheta_s)}\left(\frac{1}{R_f} - \frac{1}{R_s}\right)\frac{t_s^2}{t_f}. \qquad (1)$$

For studying the morphology of the films, a Hitachi S-4800 scanning electron microscope (SEM) (Hitachi High-Tech Co., Japan) was employed. Additionally, transmission electron microscopy (TEM) (Thermo Fisher Scientific, former FEI, Eindhoven, Netherlands), including high-resolution (HR-TEM), electron diffraction, high angle annular dark-field scanning TEM (HAADF-STEM), and electron energy loss spectroscopy (EELS) mapping studies were performed using an image aberration-corrected Titan 80-300 environmental TEM operated at 300 kV and equipped with a Gatan imaging filter Quantum 965ER (Pleasanton, USA). For the TEM studies, the samples were prepared by mechanical polishing followed by Ar^+ ion milling using a Gatan PIPS 695 setup.

The film roughness was investigated with an atomic force microscope (AFM) using a Dimension 3100 (Bruker Corporation, Billerica, MA, USA) equipped with a Nanoscope IV controller at ambient temperature in air. Standard cantilevers from Bruker (model RTESP, Santa Barbara, CA, USA) featuring a resonance frequency in the range of 315–364 kHz in air, a spring constant in the range of 20–80 N m^{-1}, and a typical tip radius of less than 10 nm were used. The scanned size was 2×2 μm^2 for the roughness calculation. Grazing incidence XRR and XRD measurements were performed in the Bragg-Brentano geometry (D8 Discover, Bruker, Germany) with Cu-Kα radiation ($\lambda = 0.154$ nm). The reflectivity curves were simulated using the Leptos software to determine the thickness, density, and roughness of the multilayers. In general, a very good agreement between the film thicknesses determined by ellipsometry, spectrophotometry, and XRR analysis has been obtained. Due to the strong crystallization of TiO_2 films at 200 °C, no reliable analysis of these films could be performed by XRR and spectrophotometry for thickness assessment.

Selected Si wafers were annealed up to 300 °C, 600 °C, and 800 °C in vacuum. The temperature was raised by 200 °C per hour, and samples were heated at the target temperature for 2 h.

Table 2. Thickness (d), density (ρ), roughness (σ), and stress values of pure metal oxide films characterized by different techniques and on different substrates. NU is the thickness non-uniformity in the ALD chamber on 6″ calculated as $(d_{\max}-d_{\min}/2d_{\text{average}})^{*}100\%$.

Substrate/ Method	d (nm) ±1% Si/Ellips	NU (%) Si/Ellips	d (nm) ±1 Si /XRR	d (nm) ±2% FS/ R,T	ρ (g cm^{-3}) ±0.1 Si /XRR	σ_{XRR} (nm) ±0.2 Si/XRR	σ_{EMA} (nm) ±0.2 Si/Ellips	σ_{AFM} (nm) ±0.1 Si/AFM	Stress (MPa) ±30 Si
Temp. 100 °C									
TiO_2	226	1.5	205	218	3.8	4.0	19.8	20.4	276
	109	2.3	107	106	3.9	0.7	1.1	0.5	230
	55	2.1	54	53	3.9	0.6	1.3	0.6	260
	29	1.9	28	—	3.8	0.6	0	0.2	289
Al_2O_3	296	1.8	—	—	—	—	0.2	0.4	260
	199	1.7	199	200	2.95	0.6	0.9	0.3	205
	102	1.8	101	100	2.95	0.6	0	0.3	268
	53	3.4	54	52	2.95	0.7	1.4	0.2	230
SiO_2	196	1.6	198	—	2.1	0.2	0	0.2	—
	101	1.1	101	—	2.2	0.3	0	0.1	—
	50	1.1	50	—	2.2	0.3	0	0.03	—
Temp. 200 °C									
Al_2O_3	185	1.5	—	—	—	—	0.7	—	150
	95	1.8	—	—	—	—	0	—	−30
	47	2.0	—	—	—	—	1.6	—	−272
TiO_2	260		—	—	—	—	—	19.8	120
	112	3.7	—	—	—	—	0.3	—	218
	67	4.7	—	—	—	—	4.2	—	511
	31	2.8	—	—	—	—	—	—	400

Table 3. Detailed film analysis of TiO_2 /Al_2O_3 and TiO_2/SiO_2 nanolaminates. (a) Slow cooling after deposition, (b) nanolaminates with Al_2O_3 as starting layer.

Substrate/Method	d (nm) ±1% Si/Ellips	NU (%) Si/Ellips	d (nm) ±1 Si/ XRR	d (nm) ±2% FS/ R,T	d (nm) ±2% BK7/ R,T	σ_{EMA} (nm) ±0.2 Si/Ellips	σ_{AFM} (nm) ±0.1 Si/AFM	Stress (MPa) ±30 Si
$[TiO_2/Al_2O_3]_x/TiO_2$								
Temp. 100 °C								
$[84/16]_{42}/24$	177	1.0	—	183	181	1.8	0.5	239
$[167/8]_{32}/10$	186	1.2	—	186	182	0.6	0.5	235
$[167/16]_{27}/10$	180	1.5	—	183	179	1.8	0.4	245
$[335/4]_{17}/300$	192	1.4	192	189	186	0.7	1.1	193
$[670/8]_{8}/630$	190	2.1	189	186	185	0.3	1.1	200
$[1340/16]_{4}/700$	190	2.1	190	189	186	0.7	1.3	193
$[1340/64]_{4}/20$	183	1.5	191	187	188	5.2	1	135
$64[1340/64]_{4}$ 20^{b}	190	2.2	—	188	183	0.1	—	235
$[1340/128]_{3}/800$	186	1.3	187	193	192	0.6	0.9	146
Temp. ⩾200 °C								
$[84/8]_{55}/20^{250}$	213	2.7	—	201	—	0.1	—	168
$[84/16]_{42}/24^{a}$	176	1.8	—	176	173	1.4	0.3	136
$[84/16]_{42}/24^{300}$	211	1.7	—	195		0.1	—	164
$16[84/16]/24^{250b}$	193	2.8	—	181	193	0.1	—	145
$[167/16]_{27}/10^{a}$	189	3.0	—	183	180	0.9	0.3	150
$[335/64]_{10}/42$	186	1.9	—	183	178	3.5	0.2	300
$[670/64]_{7}/10^{a}$	188	2.0	—	185	178	3.7	0.7	260
$[1340/64]_{4}/20$	211	4.2	—	193	192	4.3	3.9	550
$[1340/64]_{4}/20^{a}$	190	2.2	—	187		0	3.4	535
$[TiO_2/SiO_2]_x$ /TiO_2								
$[335/4]_{17}/300$	188	2.0	188	185	—	0	0.4	260
$[670/8]_{8}/630$	178	2.4	178	174	—	0	0.4	230
$[1340/16]_{4}/700$	186	1.9	187	182.6	—	0	1.1	200

All the results acquired by different techniques on different substrates are compiled in tables 2, 3 and S1 (available online at stacks.iop.org/NANO/32/095709/mmedia).

3. Results and discussion

3.1. Mechanical stress

The mechanism of mechanical stress formation in ALD coatings is still not clear. In general, the mechanical stress in thin films is influenced by various factors such as the difference between the thermal expansion coefficients of the substrate material and the coating, crystallinity and morphology of the films, the deposition temperature, and film thickness [44]. To understand the impact of the PEALD film thickness and the deposition temperature on the mechanical stress, first, a set of single-layer oxide (TiO_2, Al_2O_3, SiO_2) thin films were deposited and characterized at 100 °C and 200 °C deposition temperatures. The thicknesses of the films were varied between 30 and 300 nm. Our goal was to develop a nanolaminate composition with the highest possible refractive index but improved mechanical and optical properties than the single layers. Therefore, TiO_2 and Al_2O_3 were studied more extensively, since bulk TiO_2 and Al_2O_3 have higher refractive indices than SiO_2. Moreover, due to a strong backside deposition of the SiO_2 coatings, no reliable stress measurements could be performed for these single layers at 100 °C and were not studied at 200 °C. The optical and mechanical properties of single-layer SiO_2 [45, 46] and Al_2O_3 [10] grown by PEALD have been studied previously and are not discussed here in detail. The material properties of the single layers are summarized in table 2.

Next, the mechanical stress in ALD TiO_2/Al_2O_3 and TiO_2/SiO_2 nanolaminates have been evaluated depending on the composition of the films and time after deposition. Nanolaminates have been coated at 100 °C, 200 °C, 250 °C, and one at 300 °C with an overall target thickness of 200 nm. Their compositions and material properties are summarized in table 3.

3.1.1. Single layers. In the case of the films deposited at 100 °C, the film thickness has little influence on the measured film stress. For these TiO_2 and Al_2O_3 thin films, the tensile stress has values of around (260 ± 30) MPa and (230 ± 30) MPa, respectively, for films with a thickness between 30 and 300 nm (figure 1(a) and table 2). The variation of stress values between these single layers are within the experimental accuracy. This suggests that the mechanical stress in these coatings arises at the interface between the substrate and the coating.

At 200 °C deposition temperature, the mechanical stress values show a strong dependence on the film thickness (table 2 and figure S1). In the case of Al_2O_3, the 50 nm thin film shows compressive stress, and with increasing film thickness, tensile stress is observed; however, its magnitude is lower than for films grown at 100 °C. The tensile stress of approx. 200 nm thick Al_2O_3 film at 200 °C deposition temperature is somewhat lower

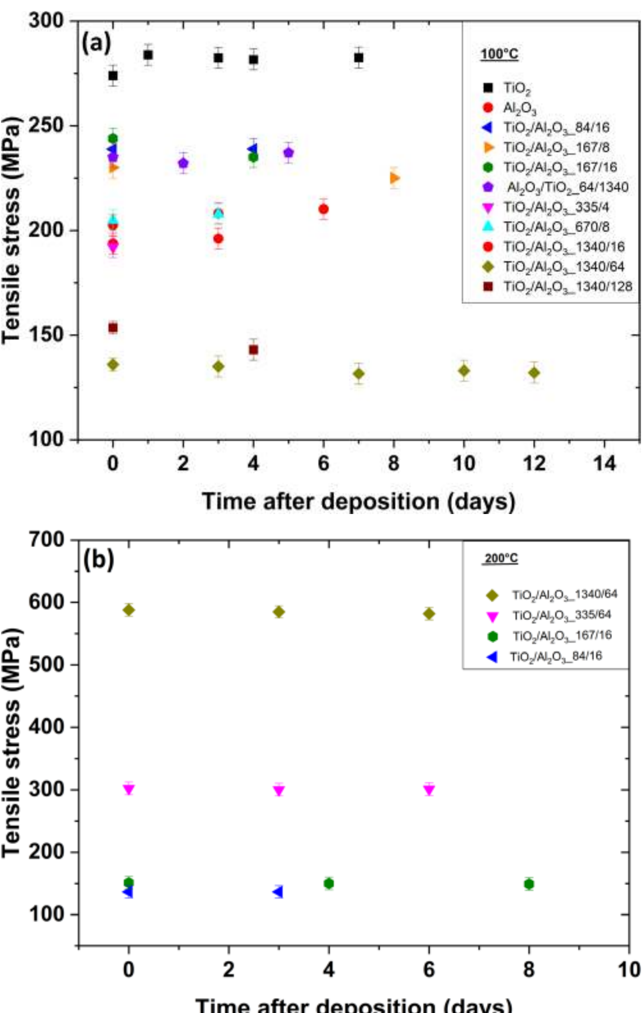

Figure 1. Mechanical stress of pure TiO_2 and Al_2O_3 layers as well as TiO_2/Al_2O_3 nanolaminates over time deposited at (a) 100 °C and, (b) 200 °C.

(150 MPa) compared to the layer grown at 100 °C (205 MPa). The further reduction of the film thickness resulted in a transition of the tensile stress to compressive stress so that around 50 nm Al_2O_3 film (corresponding to 500 ALD cycles) exhibited 272 MPa compressive stress (table 2). The TiO_2 film grown with 6666 ALD number of cycles (corresponding to a film thickness of ca. 230 nm at 100 °C and 260 nm at 200 °C) has lower mechanical stress at 200 °C than the film deposited at 100 °C. With decreasing the film thickness, the mechanical stress significantly increases (table 2). At this point, it must be emphasized that although the TiO_2 films deposited by PEALD partially crystallize already at 100 °C deposition temperature, with increasing the substrate temperature, the degree of crystallization strongly increases [8]. The low mechanical stress of thick TiO_2 films at 200 °C is attributed to the fracture and stress release in the film due to the crystallization. This assumption is confirmed by the decrease of the stress value to 0 MPa in 260 nm thick TiO_2 film during the weeks after the deposition (see figure S2). In coatings with lower thicknesses, the crystalline phase is not dominating, and both amorphous and

crystalline phases are present, resulting in a high intrinsic stress in the films.

A strong dependence of the residual stress on the film thickness during various coating processes involving high energies is attributed to the increased adatom mobility [10, 47–49]. In low energy deposition techniques, the films generally exhibit tensile stress, which does not change significantly with the film thickness. In PEALD processes, the applied energy using plasma is supplemented by the substrate temperature, increasing the overall energy at elevated deposition temperatures. Very thin films transfer the applied energy to the substrate or substrate/film interface [50].

Therefore, no significant adatom diffusion takes place in very thin films resulting in high compressive stress. With increasing thickness, the film can retain a larger amount of the supplied energy, the adatom mobility increases, resulting in stress relaxation. At a thickness $\geqslant$200 nm, the adatom mobility does not change, and the film stress stays constant [50, 51]. It is expected that this hypothesis could be further verified by a fine variation of the film thickness from several nanometers to $\geqslant$200 nm. Noteworthy, even though at 200 °C deposition temperature the thermal mismatch between substrate and the coating also increases, the impact of the adatom mobility is stronger on the overall stress in the film.

In PEALD TiO_2 coatings, the effect of the adatom mobility at higher deposition temperatures discussed above is accompanied by the film crystallization. Therefore, the stress evolution in TiO_2 is additionally correlated with the microstructural transformation with the thickness change. It was observed for various materials that during the discrete island growth, the internal stress increases reaching its maximum during the coalescence [16, 51]. The 31 nm PEALD TiO_2 film in our study has residual stress of 400 MPa, increasing to 511 MPa at a thickness of 67 nm. With further increase of the thickness to 112 nm, the stress decreases to ca. 218 MPa. It is expected that below 30 nm, the stress in PEALD $TIiO_2$ would be <400 MPa. However, for reliable measurements on very thin films, a more precise measurement technique must be applied.

The mechanical stress of TiO_2 deposited at 100 °C is higher than for Al_2O_3 thin films but considerably lower than for HfO_2 coatings reported previously to be 650 MPa [10]. The mechanical stress of HfO_2 thin films has been reduced to 450 MPa by introducing an ultra-thin Al_2O_3 layer. However, thick interference coatings still showed cracking of the films, which even propagated into the substrate material [10]. Such a large difference in the mechanical stress implies that TiO_2 ALD coatings are more eligible as high refractive index optical coatings in multilayer systems than HfO_2 if transparent coatings below 400 nm wavelength are not required for the specific applications.

Pure TiO_2 coatings using $TiCl_4$ and H_2O as a precursor have been reported to have approximately 400 MPa and 810 MPa tensile stresses grown at deposition temperatures of 110 °C and 200 °C, respectively [52]. Using the TTIP precursor and O_2 plasma as oxidizing agent, considerably lower residual stress values of below 280 MPa have been determined in this study indicating that the precursor chemistry also has a major influence on the mechanical properties of the coatings. The bonding environment but also the composition and impurities are altered by applying different oxidizing agents. Still, a similar trend of increasing the mechanical stress with decreasing the film thickness at higher deposition temperatures (200 °C for the plasma and 300 °C for the thermal processes) was also observed for a TiO_2 coating using $TiCl_4$ and H_2O [52].

Using PEALD instead of thermal ALD is another way of introducing higher energies to the surface during the deposition. The input of higher energy results in higher mobility of atoms and reduced strain in chemical bonds within the film. Consequently, amorphous PEALD coatings generally have lower residual stress than thermal coatings at the same deposition temperature, as was confirmed in our previous study for Al_2O_3 [10]. Further control of the mechanical stress in PEALD processes has been achieved by applying bias [46, 53]. By varying the average bias-voltage, the energy transfer from the energetic ions to the surface can be changed, allowing the control of the ALD material properties, including mechanical stress.

3.1.2. Nanolaminates (NL). For suppressing the crystallization in the coatings that tend to crystallize, the incorporation of thin amorphous layers of another material within the coating has proved valuable [54, 55]. Ylivaara *et al* have recently reported on nanolaminates of Al_2O_3/TiO_2 with different compositions and deposited at various temperatures with a target thickness of 100 nm [55]. By using nanolaminates, a minimum mechanical stress of 260 MPa with 50% TiO_2 content was achieved. The high content of Al_2O_3 in the nanolaminates, however, reduced the effective refractive index of the composite to below 2.2, although the pure TiO_2 layer had a refractive index of 2.4 and 2.6 at 100 °C and 200 °C, respectively.

For an application as high refractive index layers in optical coating, our goal is to reduce the residual stress in TiO_2 films by retaining its high refractive index. For this propose, a small fraction of Al_2O_3 was incorporated in the nanolaminates in this study. Whereby not only the ratio of the two components is important but also the extent of intermixing and the individual layer thicknesses.

Different compositions of the TiO_2/Al_2O_3 and TiO_2/SiO_2 were prepared at 100 °C and 200 °C to understand which parameter (ratio of the components, the extent of intermixing, or individual layer thicknesses) has a more significant effect on the residual stress in the nanolaminate coatings. The results of the stress measurements are summarized in table 3. The change in the stress value up to ten days after deposition was monitored (figure 1).

The mechanical stress of PEALD TiO_2 nanolaminates varies significantly with the composition and deposition temperature. Figures 1(a) and (b) show the mechanical stress dependence on the time after deposition for selected TiO_2/Al_2O_3 nanolaminates grown at 100 °C and 200 °C, respectively. Remarkably, mixing a few cycles of Al_2O_3 in the TiO_2 to interrupt the formation of crystallites reduces mechanical stress. Eight cycles of Al_2O_3 (corresponding to ca.1 nm) deposited after each 167 TiO_2 ALD cycles (ca. 5 nm TiO_2) leads to a reduction of the film stress from

280 MPa in pure TiO_2 film to 230 MPa in the 167/8 NL (figure 1(a)). The increase of the Al_2O_3 cycles up to16 with the same TiO_2 content does not have any significant influence on the stress value. Instead, further reduction of the residual stress was achieved by increasing the TiO_2/Al_2O_3 thickness ratio four times up to 20 nm/1 nm as in the 670/8 NL. Noteworthy, by keeping the thickness ratio and increasing the degree of intermixing of the components as in the 335/4 NL does not result in a considerable change of the overall film stress value.

An optimum ratio with the lowest mechanical stress of 135 MPa has been found for the TiO_2/Al_2O_3 NL with the cycle ratio of 1340/64, equal to a film thickness ratio of 40 nm/7.7 nm. Further increase of the Al_2O_3 thickness to 128 cycles did not influence the overall mechanical stress in the nanolaminate.

As discussed in section 3.1.1, with increasing the deposition temperature of amorphous oxide films, the residual stress can be reduced. To assess if a similar behavior is also valid for NLs, selected NLs have also been deposited at 200 °C, 250 °C and 300 °C. Comparing the stress in NL coatings with the same composition at 100 °C and 200 °C, one can see that the residual stress was considerably reduced in compositions where the thickness of TiO_2 in TiO_2/Al_2O_3 bilayer is small (in 84/16 and 167/16) (figure 1(b)). In these compositions, the stress is around 150 MPa. With increasing the number of TiO_2 ALD cycles in the bilayer, the film stress is increased to 300 MPa and ca. 600 MPa in 335/64 and 1340/64 NLs, respectively. Such an increase of the residual stress is attributed to partial crystallization of relatively thick TiO_2 components in 335/64 and 1340/64 NLs, as confirmed by XRD measurements (see section 3.3). On the other hand, in 84/16 and 167/16 nanolaminates, crystallization of TiO_2 is interrupted with 16 cycles of Al_2O_3 (2 nm) after each 2.8 nm and 5.5 nm TiO_2, respectively.

To see if the abrupt change of the temperature after the deposition also affects the overall stress value, some NLs were cooled down slowly at the rate of 20 °C h^{-1} before taking them out of the ALD chamber. As indicated in section 3.1.1, thermal stress seems to have only a minor impact on the overall stress of the coating. The 1340/64 NL has a stress value of 550 MPa if deposited at 200 °C. The same NL cooled down slowly after the deposition, has a residual stress of 535 MPa. Also, for other NLs, slow cooling resulted in a slight decrease in overall residual stress (table 3).

Further, NLs with 84 ALD cycles of TiO_2 interlayers were deposited at 250° and 300 °C. No additional improvement of the mechanical properties of these NLs was detected at elevated deposition temperatures. By starting the deposition with Al_2O_3 instead of TiO_2 did not lead to an extra reduction of the stress value at 250 °C. In a 1340/64 NL deposited at 100 °C, the stress even increased from 135 MPa to 235 MPa, if Al_2O_3 was the starting layer during the deposition (table 3).

Comparing the results in table 3, it can be concluded that the individual layer thicknesses of the components have the strongest impact on the stress values of NLs. However, the stress variation with individual layer thicknesses is reverse at 100 °C and 200 °C and can be summarized as follow:

(i) even though at 100 °C the film thickness of the single layers had no significant effect on the stress of the coatings, in NLs, the interplay of individual layer thicknesses has a strong influence on the mechanical stress. At this temperature, only in the NLs with the highest number of 1340 TiO_2 ALD cycles (ca. 44 nm) could the stress significantly be reduced. The thickness of the Al_2O_3 is also decisive for the overall stress, whereas the degree of intermixing has little influence on the mechanical performance of the NL coatings. The 44 nm TiO_2 interlayer at 100 °C is mostly amorphous (figure 2(f)), so the crystallization process does not play a significant role in the stress evolution in NLs.

(ii) At 200 °C, on the other hand, the stress is strongly influenced by the crystalization of TiO_2 (figure 3(d)). Therefore, the nanolaminates with 1340 TiO_2 ALD cycles have the highest stress values. The reduction of the stress at this temperature was achieved by reducing the number of TiO_2 ALD cycles to 84 or 167.

The mechanical properties of the SiO_2 layers significantly differ from those of the Al_2O_3 layers [10]. It was found that SiO_2 was not able to suppress mechanical stress to a great extent. All nanolaminate compositions with SiO_2 exhibited stress values between 200 and 300 MPa (table 3).

3.2. Film morphology

We have investigated the morphology and the crystallographic structure of TiO_2 PEALD coatings grown at 100 °C on Si (100) wafers. The extent of crystallinity depending on the film thickness is clearly seen in top-view SEM images (figures 2(a)–(d)). The film is mostly amorphous at lower thickness values of 29 nm and 55 nm, showing only a few small crystals on the surface. The samples were processed in ISO 5 class cleanroom, and contaminations are expected to be minimal. With increasing the film thickness to 109 nm, the size of the crystals increases (figure 2(b)). Further increase in film thickness results in an increase of the number and the size of crystals so that on the surface of 226 nm TiO_2 layer hillock shaped crystals of around 150 nm in diameter are visible (figure 2(a)). From the cross-sectional view of 226 nm film in figure (e), it is obvious that an amorphous layer initiates the ALD growth of TiO_2. There is an onset of crystallization once it reaches a certain thickness. The formation of the hillocks starts at different stages of the deposition. Hence, various sizes of the crystallites can be observed. The further increase of the film thickness results in a growth of V-shaped polycrystals within the amorphous TiO_2 film. Similar behavior of increasing the crystalline size with increasing the number of TiO_2 cycles grown by thermal ALD at higher deposition temperatures and using other precursors was also reported previously [56].

As reported previously, the crystallinity of ALD TiO_2 films can be controlled by the ALD process parameters, such as substrate temperature and plasma parameters (oxygen gas flow rate and plasma power) [8, 29]. Another approach is to interrupt the crystal growth by incorporating thin Al_2O_3 layers

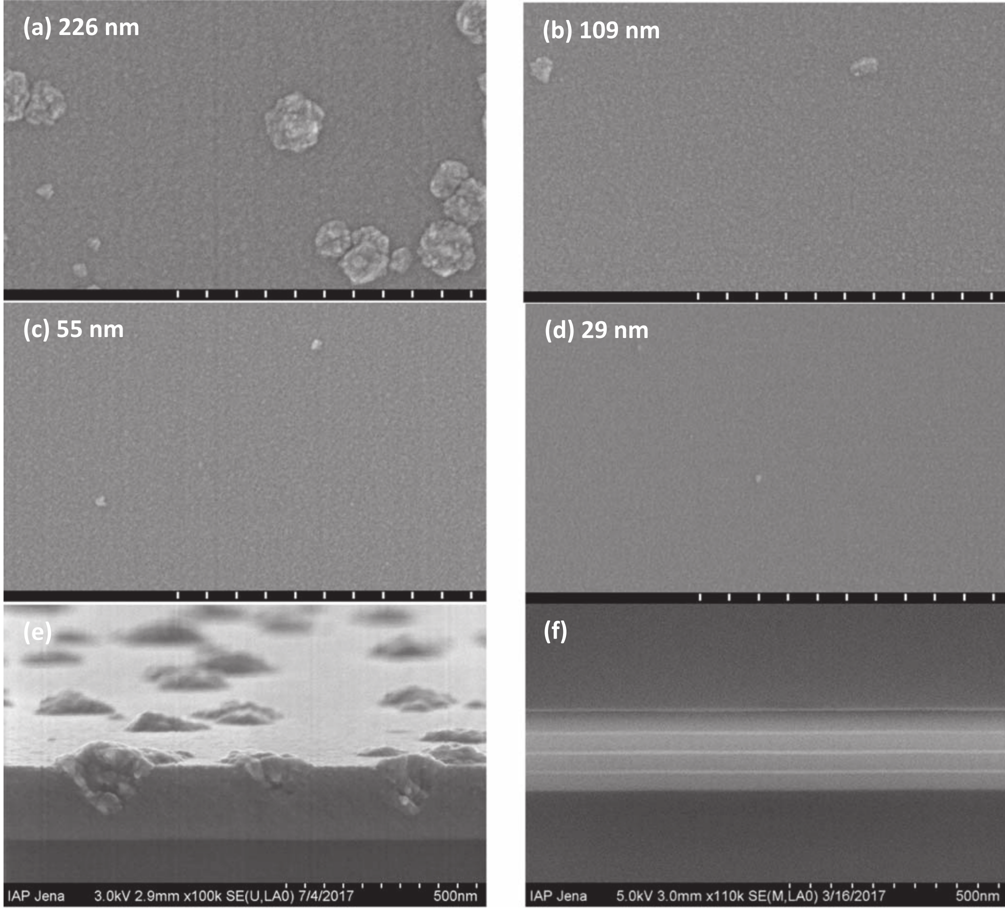

Figure 2. (a)–(d) Top-view SEM images of pure TiO_2 PEALD films grown at 100 °C with various film thicknesses. The scale bar is 1 μm. (e) and (f) Cross-sectional SEM images of 200 nm pure TiO_2 layer and TiO_2/Al_2O_3 nanolaminate with the ALD cycle ratio of 1340/64, respectively.

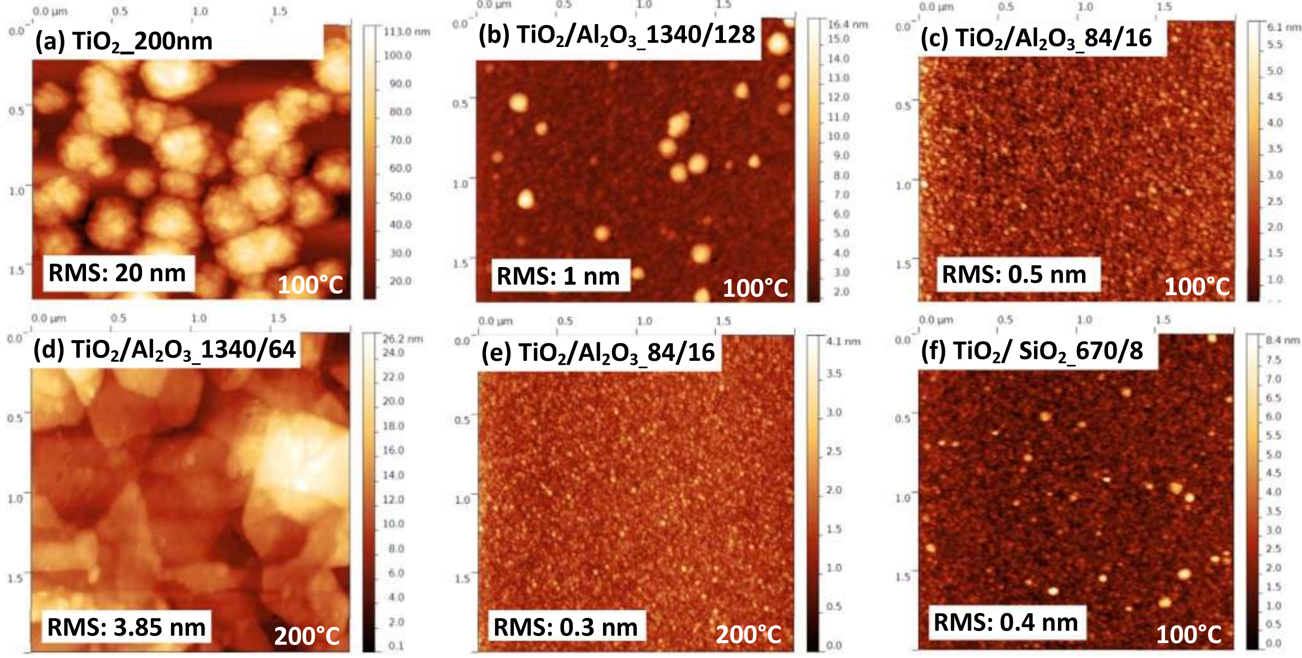

Figure 3. AFM images of (a) 200 nm TiO_2 film, (b)–(e) TiO_2/Al_2O_3 and, (f) TiO_2/SiO_2 nanolaminates grown with different cycle ratios.

into the TiO_2 film. With this approach, the crystallinity of TiO_2 coatings can be suppressed, whereas the quality of the film is maintained. Figure 2(f) displays the cross-sectional view of TiO_2/Al_2O_3 nanolaminate with a 1340/64 cycle ratio repeated four times. As can be seen, the crystallization of the TiO_2 coating could be inhibited by inserting around 7 nm Al_2O_3 after ca. 44 nm of TiO_2.

With decreasing crystallinity, the surface roughness of the coatings reduces considerably. This is explained by the difference in the growth rates of the crystalline and amorphous phases. It was reported that during the growth of TiO_2 ALD films under the same deposition conditions, the crystalline anatase phase grows faster than the amorphous TiO_2 phase [57]. The difference in growth rates of amorphous and crystalline phases is also clearly seen in the SEM image in figure 2(e). Here, during the same deposition process, a thicker crystalline phase is grown, resulting in hillock-shaped crystals within the amorphous TiO_2 surface and, consequently, an increase in surface roughness.

Quantitative analysis of the film roughness was performed by AFM and XRR measurements. Figure 3 shows the AFM images of pure TiO_2 films and selected TiO_2/Al_2O_3 and TiO_2/SiO_2 nanolaminates deposited at 100 °C and 200 °C. The root mean square (rms) roughness values of other compositions determined by AFM (σ_{AFM}) are summarized in table 3. The roughness of the 200 nm TiO_2 layer is 20 nm, as determined by AFM, with the surface being covered by numerous crystallites (figure 3(a)). The surface roughness is considerably reduced in nanolaminates to below 1.5 nm at 100 °C deposition temperature, and below 4 nm at 200 °C. The highest AFM roughness of 3.85 nm at 200 °C was determined for the nanolaminate 1340/64, which is correlated to the strong crystallization of ca 44 nm TiO_2 in each bilayer. The same composition at 100 °C has a roughness value of ca. 1 nm since, at this temperature, the crystallization of TiO_2 is considerably low (figure 2(c)). With decreasing the number of ALD TiO_2 cycles, a roughness of 0.21 nm for the 335/64 nanolaminate at 200 °C was achieved (table 3).

Further quantitative roughness analysis was conducted by XRR and using the effective medium approximation (EMA) model for ellipsometry data. Surface roughness obtained from AFM, XRR, and SE EMA layer are summarized in table 2 for single layers, and tables 3 and S1 for nanolaminates. The different roughness values obtained by these techniques can be attributed to the measurement characteristics of the methods and was also reported previously [58].

Detailed XRR analysis was further conducted on Si substrates to understand the formation of multilayers. Experimental and simulated curves of selected samples are presented in figures 4 and S3. Bilayers in the nanolaminates are clearly visible with the lowest (4 ALD cycles) number of Al_2O_3 cycles in figure 4. It is evident that Al_2O_3 retains its individuality in nanolaminates even at 0.5 nm thickness, indicating bilayer uniformity with sharp interfaces. The individual layer thicknesses, roughness, and density for certain nanolaminate compositions obtained from XRR

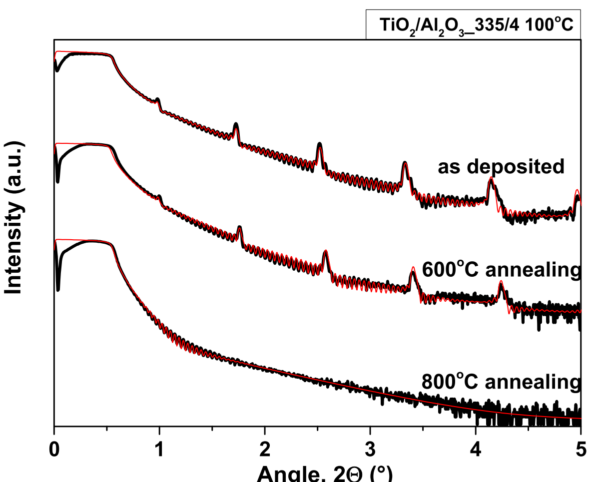

Figure 4. XRR measured (black) and simulated curves (red) of the TiO_2/Al_2O_3 335/4 nanolaminate. Diffractograms are vertically shifted for the sake of clarity.

measurements are presented in table S1. It was found that the density of Al_2O_3 increased from 2.0 to 3.1 g cm^{-3} with increasing the number of ALD cycles. Comparing the same cycle compositions, SiO_2 showed less variation in density.

Further, the XRR results indicate that the obtained overall thickness is in good correlation with the film thickness acquired by ellipsometry. The difference between the thickness measured by ellipsometry and XRR for each sample ranges from 0.1 to 7.5 nm (<0.5% of the film thickness). The 200 nm film thickness target has not been achieved due to deviations in film growth and nucleation on different substrates.

3.3. Annealing

XRD and XRR analysis were used to evaluate the structural transformation of TiO_2 and TiO_2/Al_2O_3 nanolaminate thin films as a function of the annealing temperature. We annealed three different samples in order to understand how the TiO_2 content in the PEALD grown nanolaminate affects the crystallinity of the film. We first examined TiO_2 with 50 nm thickness and TiO_2/Al_2O_3 nanolaminate with a cycle ratio of 335/4 grown at 100 °C. Among depositions at a higher temperature, TiO_2/Al_2O_3 1340/64 NL grown at 200 °C was analyzed as it has the highest number of TiO_2 cycles equivalent to 40 nm in one bilayer. Figure 5 shows the XRD results before and after annealing of the films at temperatures of 300 °C, 600 °C, and 800 °C on silicon substrates. The XRD results indicate that the as-deposited 50 nm pure TiO_2 film is amorphous and remained amorphous up to 300 °C as no peak could be found in XRD patterns (figure 5(a)). At 600 °C, the (101) peak demonstrates the formation of the anatase phase in pure TiO_2 film. By increasing the annealing temperature from 600 °C to 800 °C, further peaks appear at 25.2° (101), 53.9° (105), and 55.1° (211) 2Θ angles indicating the formation of the anatase phase with a tetragonal crystal structure. No rutile TiO_2 phase was detected. TiO_2/Al_2O_3 335/4 NL displays the onset of crystallization at 600 °C with prominent peaks (101),

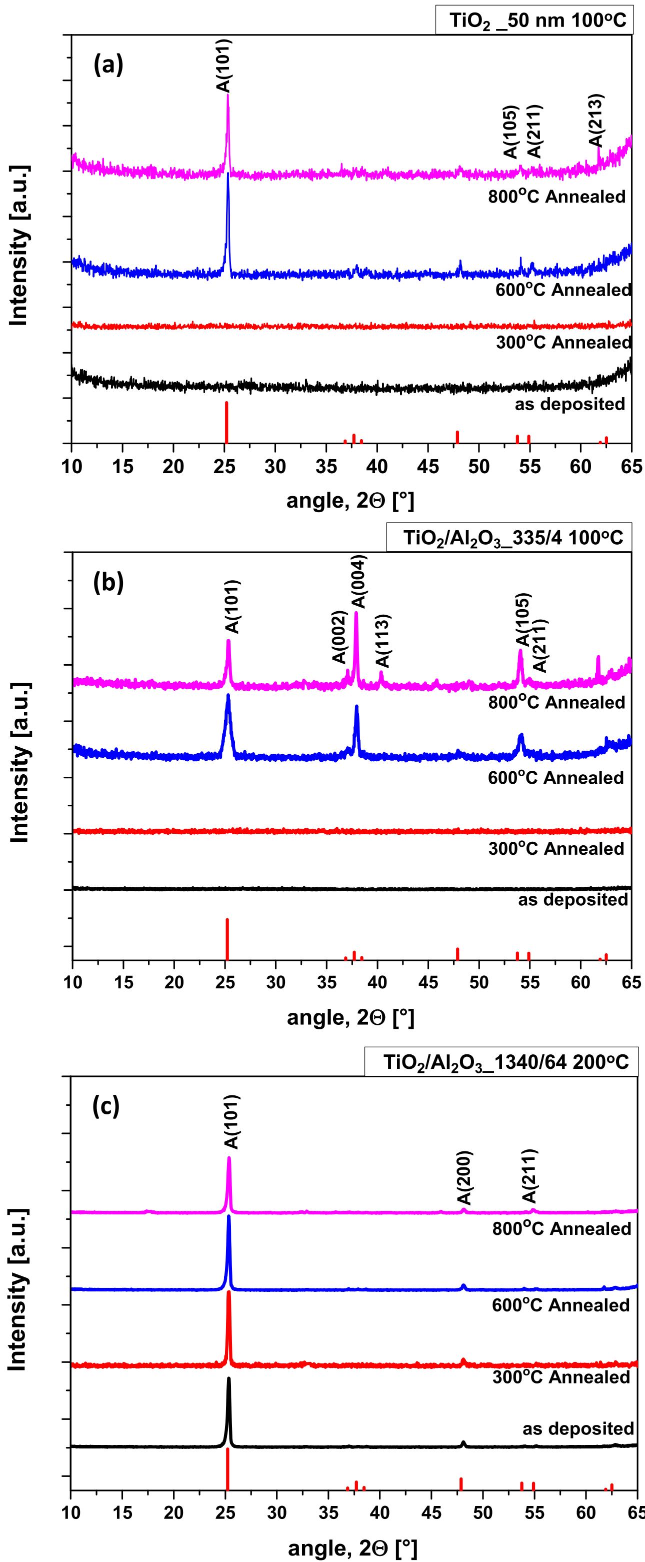

Figure 5. XRD patterns of thin films (a) TiO_2, TiO_2/Al_2O_3 nanolaminates with cycle ratio of (b) 335/4 and (c) 1340/64 compared with the effect of annealing temperature on structural properties of nanolaminate films deposited at (a), (b) 100 °C and (c) 200 °C. The red column bars mark anatase peaks [59].

(004), (105), and additional peaks (002), (113), (211) after annealing at 800 °C (figure 5(b)). At 200 °C deposited TiO_2/Al_2O_3 1340/64 NL shows crystalline behavior already after deposition. The anatase peaks (101) and (200) are retained on annealing at 600 °C and 800 °C (figure 5(c)). No peaks related to Al_2O_3 were observed, indicating the amorphous nature of the Al_2O_3 in the NLs.

TEM images of as-grown 335/4 coating are shown in figure 6(a). The sharp and flat layers of TiO_2 and Al_2O_3 are clearly visible in the HAADF image, and the distribution of Al and Ti is confirmed by EELS mapping (shown in the inset). All layers are mainly amorphous; however, a small amount of nanocrystals is found in the TiO_2 layers.

Upon annealing at 800 °C, the coating is transformed into a polycrystalline film shown in figure 6(c). The large single

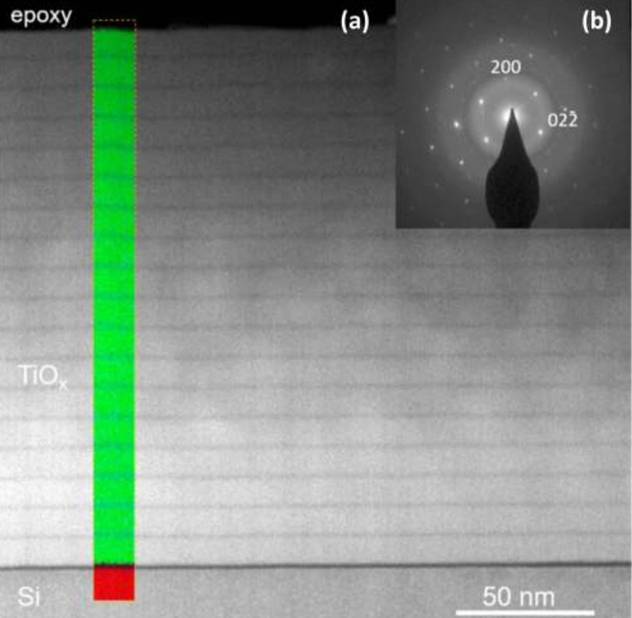

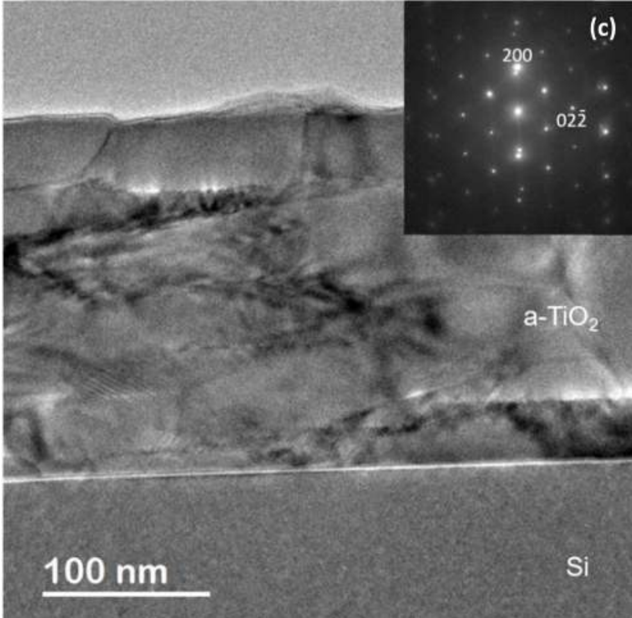

Figure 6. Transmission electron microscopy images of the TiO_2/Al_2O_3 335/4 sample (a), (b) as deposited and (c) after annealing at 800 °C. Electron diffractions shown as insets display sharp spots from the Si substrate and additional spots from the anatase TiO_2.

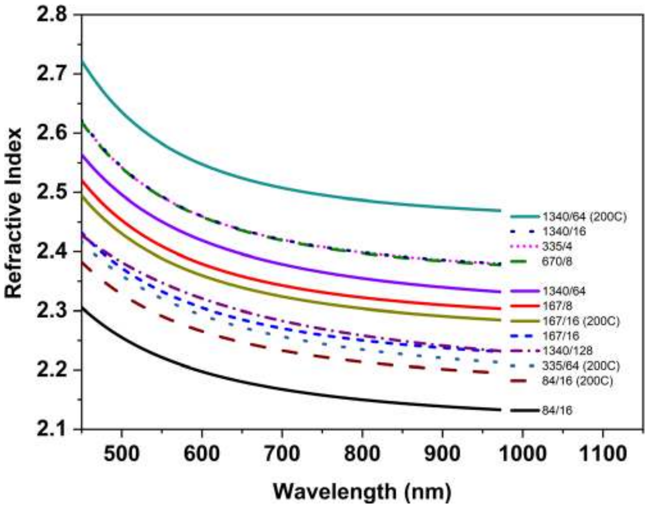

Figure 7. Refractive index variation of TiO_2/Al_2O_3 nanolaminates grown at 100 °C and 200 °C measured on Si substrate.

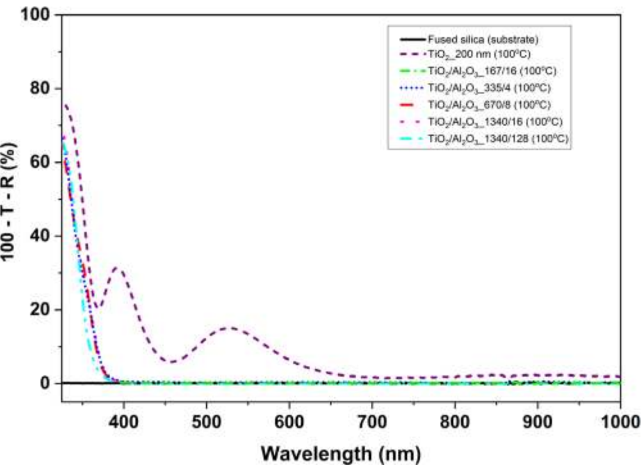

Figure 8. Optical losses of pure TiO_2 film and selected nanolaminates deposited at 100 °C.

crystal grains having the structure of the TiO_2 anatase phase (space group I 4(1)/amd) are formed. The layers of Al_2O_3 are not visible, revealing the strong diffusion of elements during the annealing process.

The mixing of Al_2O_3 and TiO_2 layers into each other in 335/4 nanolaminate after annealing the film at 800 °C was also confirmed by XRR measurements (figure 4). The periodic nanolaminate structure is still detectable at 600 °C annealing temperature, which then disappears after annealing at 800 °C.

3.4. Optical properties

The optical constants of the nanolaminates have been compared depending on the deposition temperature, composition, and substrate material. On Si substrates, the refractive indices were calculated by fitting with SE measured data of Ψ and Δ with a Cauchy model with the extinction coefficient set as $k = 0$. Several observations can be made by comparing the refractive indices of nanolaminates shown in figure 7: (i) the higher is the number of Al_2O_3 ALD cycles in nanolaminates at the same deposition temperature, the lower is the refractive index (e.g. 167/8 versus 167/16); (ii) the same composition deposited at 200 °C has a higher refractive index than at 100 °C temperature (e.g. 84/16 at 100 °C and 200 °C); (iii) the refractive indices of films with the same amount of TiO_2 and Al_2O_3 but different bilayer thickness are overlapping if deposited at 100 °C (such as NLs 335/4, 670/8 and 1340/16), whereas at 200 °C deposition temperature, there is a slight difference.

(i) The decrease of the nanolaminate refractive index is due to the lower refractive index of pure Al_2O_3 films being 1.62, whereas pure TiO_2 has a refractive index of 2.4 at 100 °C. When the number of TiO_2 cycles was reduced to 167, the refractive index was 2.36 with just 8 cycles of Al_2O_3 and reduced further to 2.30 when Al_2O_3 cycles were doubled, i.e. the ratio was reduced to half. The refractive index eventually dropped to 2.18 when the cycle ratio was halved to 84/16. A similar trend was observed for nanolaminates at 200 °C. Pure TiO_2 deposited at 200 °C with a thickness of 67 nm reported a refractive index of 2.53 from SE measurements.

(ii) TiO_2/Al_2O_3 1340/64 deposited at 200 °C has a refractive index of 2.53, the highest value of all the nanolaminates. Other compositions at the same temperature showed lower refractive indices in the range of 2.34–2.27, on account of decreased cycle ratio. The increase of the refractive index with the substrate temperature is connected to the increased mobility and dense packing of atoms and molecules in the films. As a result, the film density increases and, according to the Lorentz–Lorenz equation, the refractive index also increases.

(iii) Even though the ALD cycle ratio in the nanolaminates 335/64 and 84/16 is the same, the refractive index of the 335/64 is higher than that of the 84/16 at 200 °C deposition temperature. This can be attributed to the higher crystallization degree of 335/64 composition due to the thicker TiO_2 in a bilayer.

Optical losses of TiO_2 at 100 °C and selected nanolaminates are presented in figure 8. Losses are caused by the intensity reduction of transmitted light due to absorption or scattering. Optical loss is considered to be an essential parameter while designing thin-film optical systems and should be as small as possible. Spectrophotometry results gave an insight to the homogeneity of the films and the corresponding optical losses. The latter is calculated from transmittance T, and reflectance R measurements of deposited thin films as 100%-T–R. Reflectance and transmittance spectra of TiO_2 in the wavelength range of 200–1200 nm showed that films are not homogenous. At 200 nm thickness, high optical losses were evidently arising from scattering losses due to the crystalline nature of the coatings, as confirmed by AFM (figure 3 (a)). Further, for 50 and 100 nm films, optical losses diminished. Below 400 nm, the optical losses increased on account of the band transition of TiO_2 ($E_g = 3.3$ eV) (figure 8). In contrast, low optical losses and high film

homogeneity were achieved in all nanolaminate compositions (figure 8). The results show that high refractive index films with low optical losses can be realized by incorporating amorphous Al_2O_3 into TiO_2 films.

3.5. Narrow band pass filter (NBF)

NBF comprising of a high and low refractive index interference stack with a total thickness of ca. 1.8 μm was realized. We aimed to evaluate the mechanical and optical performance of the stress-optimized nanolaminates in a complex optical system coated on various substrates. The optical function of NBF coatings is not the scope of the work and will not be discussed in detail. As a high refractive index component, the nanolaminate TiO_2/Al_2O_3 84/16 with the combination of the lowest residual stress (136 MPa) (figure 1(b)) and roughness (rms 0.3 nm) (figure 3(e)) at 200 °C was chosen. SiO_2 was used as a low refractive index layer. The cross-sectional SEM image on the Si substrate in figure 9(a) shows the distinct layers of the high and low refractive index materials, including around 190 nm SiO_2 spacer layer in the middle. No cracks or damage of the coating was detected on Si substrates as well as on lenses. Whereas on plane FS substrates, cracks in the coating were seen under the optical microscope. This implies that even though the mechanical properties of high refractive index TiO_2 coatings were considerably improved using nanolaminates, further developments are still necessary to obtain crack-free optical coatings independent of the substrate material.

The reflectance spectra in figure 9(b) confirm the conformal coating on a half-ball FS lens. The shift of the peak is merely 3 nm (from 557 to 560 nm, shown as inset), depending on the position on the lens. Similarly good results were also achieved on the ball and aspherical lenses. The targeted bandpass transmittance peak at 532 nm was not met. However, it must be emphasized that NBF was deposited by using the GPC values of individual single layers on Si. However, the GPC of ALD layers depends on the substrate (table 3) and on the underlying material on which the film grows. For the precise assessment of the number of ALD cycles for getting the desired film thickness, a detailed growth rate analysis of single layers is still required.

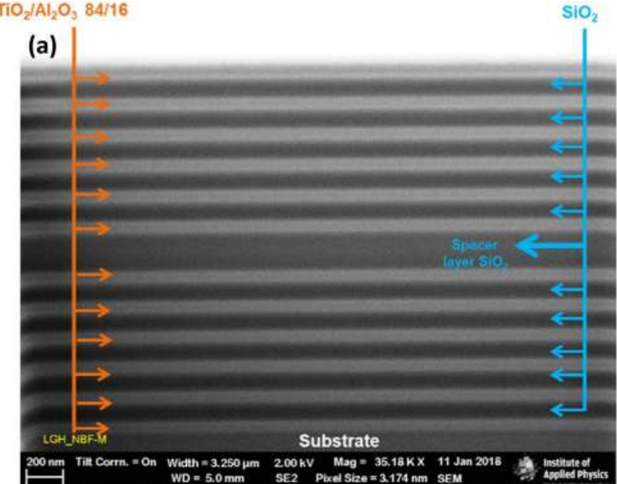

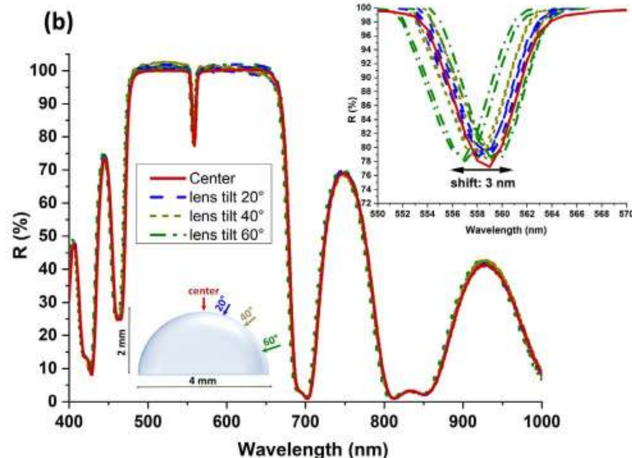

Figure 9. (a) Cross-sectional SEM micrograph of the NBF on Si substrate, (b) reflectance spectra on a coated lens measured at the angle of normal incidence (AOI = 0°) at 20°, 40°, and 60° tilting angles of the lens (four opposite points at each angle). (Inset) variation of the peak position between 550 and 570 nm depending on the position on the lens.

4. Conclusion

This article presents a comprehensive study of TiO_2 nanolaminates for optical coatings. With only a few cycles of Al_2O_3, the crystallization of TiO_2 could be suppressed to achieve optical TiO_2 coatings with properties superior to that of the pure TiO_2. These properties depend on the growth temperature and individual layer thicknesses, which have a substantial impact on the surface roughness and residual stress. Thin films with the lowest residual stress of 136 MPa was achieved in the TiO_2/Al_2O_3 84/16 nanolaminate deposited at 200 °C. The higher deposition temperature was also favorable for a nanolaminate coating with a high refractive index of 2.35. With SiO_2 thin layers within the TiO_2, no significant reduction of the residual stress was observed, although pure PEALD SiO_2 has a significantly lower mechanical stress compared to PEALD Al_2O_3 [10]. The experimental analysis by XRR and AFM revealed that smooth films with rms roughness below 1 nm were obtained with both Al_2O_3 and SiO_2 layers. Composite films with 4 ALD cycles of Al_2O_3 within 335 cycles of TiO_2 exhibited distinct, nanolaminate-like structure as confirmed by XRR and HRTEM. The TiO_2/Al_2O_3 nanolaminates are thermally stable up to 600 °C.

Using the acquired knowledge about the mechanical, structural, and optical properties of TiO_2 nanolaminates, a NBF with very good conformality was realized on various substrates.

In this study, lower residual stress in high refractive index TiO_2 coatings was achieved by PEALD than reported previously for thermal ALD. The advantage of the PEALD is that it allows the deposition of high-quality coatings at lower deposition temperature. Further improvement of the nanolaminate properties can be achieved by applying bias during the PEALD process.

Acknowledgments

This work was financially supported by the Deutsche Forschungsgemeinschaft (DFG, German Research Foundation) Emmy Noether project SZ 253/1-1, DFG-Priority Programme Fields Matter SPP1959/1 within the projects SZ253/2-1 and RO 5387/1-1, DFG Sonderforschungsbereich (SFB) 1375 NOA, Fraunhofer IOF Center of Excellence in Photonics and by the Fraunhofer Society within the Attract 066-601020 project.

ORCID iDs

Lilit Ghazaryan https://orcid.org/0000-0001-9979-5541
Paul Schmitt https://orcid.org/0000-0003-4298-9438
Vivek Beladiya https://orcid.org/0000-0002-8094-6300
Adriana Szeghalmi https://orcid.org/0000-0003-2055-2825

References

[1] Hamann T W, Martinson A B F, Elam J W, Pellin M J and Hupp J T 2008 *J. Phys. Chem.* C **112** 10303–7
[2] Kemell M, Pore V, Tupala J, Ritala M and Leskelä M 2007 *Chem. Mater.* **19** 1816–20
[3] Wang J, Bai Y, Wu M, Yin J and Zhang W F 2009 *J. Power Sources* **191** 614–8
[4] Siefke T, Kroker S, Pfeiffer K, Puffky O, Dietrich K, Franta D, Ohlídal I, Szeghalmi A, Kley E-B and Tünnermann A 2016 *Adv. Opt. Mater.* **4** 1780–6
[5] Dominik M, Leśniewski A, Janczuk M, Niedziółka-Jönsson J, Hołdyński M, Wachnicki Ł, Godlewski M, Bock W J and Śmietana M 2017 *Biosens. Bioelectron* **93** 102–9
[6] Szeghalmi A, Helgert M, Brunner R, Heyroth F, Gösele U and Knez M 2009 *Appl. Opt.* **48** 1727–32
[7] Zaitsu S-I, Jitsuno T, Nakatsuka M, Yamanaka T and Motokoshi S 2002 *Appl. Phys. Lett.* **80** 2442–4
[8] Ratzsch S, Kley E-B, Tünnermann A and Szeghalmi A 2015 *Nanotechnology* **26** 24003
[9] Abadias G, Chason E, Keckes J, Sebastiani M, Thompson G B, Barthel E, Doll G L, Murray C E, Stoessel C H and Martinu L 2018 *J. Vac. Sci. Technol.* A **36** 20801
[10] Shestaeva S, Bingel A, Munzert P, Ghazaryan L, Patzig C, Tünnermann A and Szeghalmi A 2017 *Appl. Opt.* **56** C47–59
[11] Damberga D, Viter R, Fedorenko V, Iatsunskyi I, Coy E, Graniel O, Balme S, Miele P and Bechelany M 2020 *J. Phys. Chem.* C **124** 9434–41
[12] Elam J W, Routkevitch D, Mardilovich P P and George S M 2003 *Chem. Mater.* **15** 3507–17
[13] Pfeiffer K, Ghazaryan L, Schulz U and Szeghalmi A 2019 *ACS Appl. Mater. Interfaces* **11** 21887–94
[14] Pfeiffer K, Schulz U, Tünnermann A and Szeghalmi A 2017 *Coatings* **7** 118
[15] Szeghalmi A, Sklarek K, Helgert M, Brunner R, Erfurth W, Gosele U and Knez M 2010 *Small* **6** 2701–7
[16] Floro J A, Chason E, Cammarata R C and Srolovitz D J 2002 *MRS Bull.* **27** 19–25
[17] Weber M, Julbe A, Ayral A, Miele P and Bechelany M 2018 *Chem. Mater.* **30** 7368–90
[18] Ghazaryan L, Kley E-B, Tünnermann A and Szeghalmi A 2016 *Nanotechnology* **27** 255603
[19] Ghazaryan L, Kley E-B, Tünnermann A and Viorica Szeghalmi A 2013 *J. Vac. Sci. Technol.* A **31** 01A149
[20] Aghaee M, Maydannik P S, Johansson P, Kuusipalo J, Creatore M, Homola T and Cameron D C 2015 *J. Vac. Sci. Technol.* A **33** 41512
[21] Dickey E, Niiranen K, Danforth B and Barrow W A 2020 *Appl. Opt.* **59** A16–9
[22] Muñoz-Rojas D, Maindron T, Esteve A, Piallat F, Kools J C S and Decams J-M 2019 *Mater. Today Chem.* **12** 96–120
[23] Poodt P, Cameron D C, Dickey E, George S M, Kuznetsov V, Parsons G N, Roozeboom F, Sundaram G and Vermeer A 2012 *J. Vac. Sci. Technol.* A **30** 10802
[24] Niemelä J-P, Marin G and Karppinen M 2017 *Semicond. Sci. Technol.* **32** 93005
[25] Graniel O, Weber M, Balme S, Miele P and Bechelany M 2018 *Biosens. Bioelectron.* **122** 147–59
[26] Chawla V, Ruoho M, Weber M, Chaaya A A, Taylor A A, Charmette C, Miele P, Bechelany M, Michler J and Utke I 2019 *Nanomaterials* **9** 88
[27] Puurunen R L, Sajavaara T, Santala E, Miikkulainen V, Saukkonen T, Laitinen M and Leskelä M 2011 *J. Nanosci. Nanotechnol.* **11** 8101–7
[28] Dufond M E, Diouf M W, Badie C, Laffon C, Parent P, Ferry D, Grosso D, Kools J C S, Elliott S D and Santinacci L 2020 *Chem. Mater.* **32** 1393–407
[29] Lee W-J and Hon M-H 2010 *J. Phys. Chem.* C **114** 6917–21
[30] Chiappim W, Testoni G E, Doria A C O C, Pessoa R S, Fraga M A, Galvão N K A M, Grigorov K G, Vieira L and Maciel H S 2016 *Nanotechnology* **27** 305701
[31] Ritala M, Leskeli M, Niinistö L, Prohaska T, Friedbacher G and Grasserbauer M 1994 *Thin Solid Films* **249** 155–62
[32] Mitchell D R G, Triani G, Attard D J, Finnie K S, Evans P J, Barbé C J and Bartlett J R 2006 *Smart Mater. Struct.* **15** S57–64
[33] Testoni G E, Chiappim W, Pessoa R S, Fraga M A, Miyakawa W, Sakane K K, Galvão N K A M, Vieira L and Maciel H S 2016 *J. Phys. D: Appl. Phys.* **49** 375301
[34] Zhang G Z, Wu H, Chen C, Wang T, Wang P Y, Mai L Q, Yue J and Liu C 2014 *Appl. Phys. Lett.* **104** 163503
[35] Han D-S, Choi D-K and Park J-W 2014 *Thin Solid Films* **552** 155–8
[36] Kim L H, Jeong Y J, An T K, Park S, Jang J H, Nam S, Jang J, Kim S H and Park C E 2016 *Phys. Chem. Chem. Phys* **18** 1042–9
[37] Wang W-C, Tsai M-C, Yang J, Hsu C and Chen M-J 2015 *ACS Appl. Mater. Interfaces* **7** 10228–37
[38] Kim Y S and Jin Yun S 2005 *J. Cryst. Growth* **274** 585–93
[39] Garces N Y, Meyer D J, Wheeler V D, Liliental-Weber Z, Gaskill D K and Eddy C R 2014 *J. Vac. Sci. Technol.* B **32** 03D101
[40] Ali S, Juntunen T, Sintonen S, Ylivaara O M E, Puurunen R L, Lipsanen H, Tittonen I and Hannula S-P 2016 *Nanotechnology* **27** 445704
[41] Maula J, Härkönen K and Nikolov A 2006 Multilayer material and method of preparing same Patent number: EP 1 674 890 A2
[42] Iatsunskyi I, Coy E, Viter R, Nowaczyk G, Jancelewicz M, Baleviciute I, Załęski K and Jurga S 2015 *J. Phys. Chem.* C **119** 20591–9
[43] Stoney G G 1909 *Proc. R. Soc.* A **82** 172–5
[44] Strauss G N 2003 Mechanical stress in optical coatings *Optical Interference Coatings* (*Springer Series in Optical Sciences* vol 88) ed N Kaiser and H K Pulker (Berlin: Springer) pp 207–29
[45] Pfeiffer K *et al* 2016 *Opt. Mater. Express* **6** 660
[46] Beladiya V *et al* 2020 *Nanoscale* **12** 2089–102

[47] Proost J and Spaepen F 2002 *J. Appl. Phys.* **91** 204
[48] Ylivaara O M E *et al* 2014 *Thin Solid Films* **552** 124–35
[49] Tripp M K, Stampfer C, Miller D C, Helbling T, Herrmann C F, Hierold C, Gall K, George S M and Bright V M 2006 *Sensors Actuators* A **130–131** 419–29
[50] Strauss G N, Danh N Q and Pulker H K 1997 *J. Non-Cryst. Solids* **218** 256–61
[51] Mbam S O, Nwonu S E, Orelaja O A, Nwigwe U S and Gou X-F 2019 *Mater. Res. Express* **6** 122001
[52] Lyytinen J *et al* 2015 *Wear* **342–343** 270–8
[53] Faraz T *et al* 2018 *ACS Appl. Mater. Interfaces* **10** 13158–80
[54] Hausmann D M and Gordon R G 2003 *J. Cryst. Growth* **249** 251–61
[55] Ylivaara O M E *et al* 2017 *J. Vac. Sci. Technol.* A **35** 01B105
[56] Alekhin A P, Gudkova S A, Markeev A M, Mitiaev A S, Sigarev A A and Toknova V F 2010 *Appl. Surf. Sci.* **257** 186–91
[57] Aarik J, Karlis J, Mändar H, Uustare T and Sammelselg V 2001 *Appl. Surf. Sci.* **181** 339–48
[58] Aarik L, Arroval T, Rammula R, Mändar H, Sammelselg V, Hudec B, Hušeková K, Fröhlich K and Aarik J 2014 *Thin Solid Films* **565** 19–24
[59] Swanson H E, McMurdie H F, Morris M C and Evans E H 1969 *Standard X-Ray Diffraction Powder Patterns* (Maryland, U.S.: U.S. Department of Commerce, National Bureau of Standards) Monogr. 25, section 7